ACS APPLIED MATERIALS & INTERFACES

Research Article

www.acsami.org

Hydrothermal Synthesis of Self-Assembled Hierarchical Tungsten Oxides Hollow Spheres and Their Gas Sensing Properties

Jinwei Li,[†] Xin Liu,[†,‡] Jiashan Cui,[†] and Jianbo Sun*[,†]

[†]Key Laboratory for Photonic and Electronic Bandgap Materials, Ministry of Education, School of Physics and Electronic Engineering, Harbin Normal University, Harbin 150025, P. R. China

[‡]Department of Physics, Harbin Institute of Technology, Harbin 150001, P. R. China

Supporting Information

ABSTRACT: Hierarchical self-assembled hollow spheres (HS) of tungsten oxide nanosheets have been synthesized via a template-free hydrothermal method. Morphology evolution of the products is determined by the amount of $H_2C_2O_4$ (oxalic acid) which serves as chelating agent. Structural features of the products were characterized by X-ray diffraction (XRD), and morphology was investigated by scanning electron microscopy (SEM) and transmission electron microscopy (TEM). In addition, the porous structure was analyzed using the Brunauer–Emmett–Teller (BET) approach. The synthesis mechanism of the products with self-assembled hierarchical structures was proposed. The NO_2 gas sensing properties of self-assembled hierarchical WO_3 HS materials were investigated, the gas sensing properties of WO_3 synthesized by a variety of formulations were compared, and the possible gas sensing mechanism was discussed. The obvious enhancement of the gas sensing properties was ascribed to the structure of the hierarchical HS.

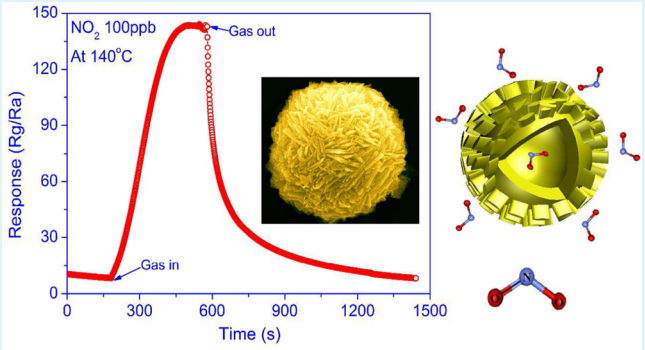

KEYWORDS: *WO_3, hierarchical hollow spheres, gas sensing properties, oxalic acid*

INTRODUCTION

WO_3 is an important semiconductor functional material with the advantages of the wide gap, nontoxicity, and abundant sources. It is used in lithium-ion batteries,[1] photocatalysts,[2] solar energy devices,[3] and photoelectrochemistry.[4] In the field of gas sensor applications, WO_3, ZnO,[5] and SnO_2[6] were used widely. Particularly, WO_3 plays an important role in detecting toxic and harmful gases such as NO_2,[7] NH_3,[8] and C_3H_6O (acetone).[9] Studies indicate that large surface area and nanostructure have a great contribution in the gas detection. To date, various WO_3 nanostructures have been reported, such as nanoparticles,[10] nanorods,[11] nanowires,[12] nanosheets,[13] and nanoflowers,[14] produced by various methods. Among different nanostructures, the hierarchical 3D (three-dimensional) architectures, which are composed by low dimension nanoscale blocks, attract great attention for the gas sensor applications.[15−17] Such a structure usually has a large surface area, so that plenty of active sites can be provided. The favorable paths for the effective reaction and diffusion of the examined gas are provided by the hierarchical architecture. Such structural characteristics are in favor of the adsorption and desorption of the detected gas.[18] As a consequence, they can lead to gas sensing properties superior to other structures. As a typical representative structure, hollow sphere (HS) has been synthesized successfully by various strategies, which can be roughly divided into four categories that involve not only conventional means such as soft-templating[19] and hard-templating[20] approaches, but also emerging novel methods such as free-templating and sacrificial-templating.[21] Among them, hard-templating, soft-templating, and sacrificial-templating methods need high-temperature calcination and acid or alkali washing to remove the template. It is easy to damage an HS structure and introduce impurity ions in the process. However, the free-template method does not require template removal, which has an advantage of keeping the HS structure undisturbed.

In this paper, self-assembled hierarchical HS of WO_3 single-crystalline nanosheets were obtained through a free-template mild hydrothermal approach. $H_2C_2O_4$ acts as the chelating agent during the hydrothermal growth. A sensor based on the as-synthesized WO_3 HS was also measured.

EXPERIMENTAL SECTION

2.1. Synthesis of the Products. All of the chemicals used were of analytical grade, purchased from Sigma-Aldrich. The synthesis was performed as follows. First 6.12 mmol of sodium tungstate (99.5% purity) was dissolved in 12.5 mL of DW (distilled water) by magnetic stirring. A yellow precursor solution was formed by slowly adding 12.5

Received: November 19, 2014
Accepted: April 28, 2015
Published: April 28, 2015

DOI: 10.1021/am508121p
ACS Appl. Mater. Interfaces 2015, 7, 10108−10114

mL of HCl (37%) solution (2 mol/L) to the obtained transparent solution. Then the mixture of $H_2C_2O_4$ (99.5% purity, 1.53 mmol) and DW (25 mL) was added to the precursor solution. Subsequently, the mixture solution was poured into a hydrothermal synthesis reactor and kept at 90 °C for 3 h. The obtained yellow precipitate was rinsed using DW and ethanol for 5 times, and after that dried in vacuum at 60 °C for 12 h. Eventually, the self-assembled hierarchical WO_3 HS was achieved by calcining the products at 500 °C for 1 h in air. For comparison, a range of specimens could be obtained by varying hydrothermal times, molar ratio of $H_2C_2O_4$ to sodium tungstate, or annealing temperatures, while other conditions were kept unchanged. All the experimental parameters can be seen in Tables S1 and S2 in the Supporting Information (SI).

2.2. Characterization. The crystallographic structure of the powders was resolved by X-ray diffraction (XRD) on the Rigaku D/max2600 diffractometer using CuKα radiation, wavelength 1.5418 Å in the 2θ range from 20° to 70°. The morphological characterization was carried out with a Hitachi SU70 field-emission scanning electron microscope (FE-SEM). Transmission electron microscopy (TEM), selected-area electron diffraction (SAED), and high-resolution transmission electron microscopy (HRTEM) measurements were performed on a FEI Tecnai F20 microscope at 200 kV. The pore size distribution and the surface area were derived using the Brunauer–Emmett–Teller (BET) method.

2.3. Gas Sensor Fabrication and Measurements. Gas sensors can be manufactured according to the following procedures. Make a paste by grinding the mixture of 10 mg of the obtained powder and DW, and further coat a ceramic tube (the surface of which is attached by a couple of gold electrodes firmly fixed together with two Pt wires) with the paste. Testing was performed in static atmosphere, in a 10 L chamber. The air from the environmental atmosphere was used as the reference gas. Using an injector, an amount of the tested target gas was rapidly injected into the test chamber. For NO_2, CO, or H_2 gases, the required concentration of the examined gases was achieved by mixing the standard gas and air of the known volume. The required concentration of acetone and ethanol was obtained by evaporating certain volumes of liquid acetone and ethanol in the chamber. The sensor was then put in the chamber in order to test its performance. After the value of the sensor's resistance stayed stable in air, the sensor was transferred to the chamber containing target gas to get another stable resistance value. An accurate digital multimeter (Fluke, 8846A) was connected to a data acquisition computer, which allowed monitoring of the sensor's resistance when it was in the air or in the target gas chamber. The temperature of the test atmosphere was 20 °C and its humidity was 10% RH. Parameters Rg/Ra and Ra/Rg, corresponding to the oxidizing and the reducing gas, respectively, are defined as the sensor response. Here, Ra and Rg represent the dynamic resistance when the sensor is in the air and in the target gas, respectively. In addition, when the sensor was moved from air to the examined gas (for example oxidizing gas), the response time was defined as the time at which the resistance reached 90% of its steady value. The recovery time was defined as the time during which the resistance returned to 10% of the steady value, after the sensor had been removed from the examined gas.

RESULTS AND DISCUSSION

3.1. Structure and Morphology. XRD analysis is usually used to resolve samples' crystal structures. As can be seen in the obtained XRD patterns (Figure 1), all diffraction peaks are highly consistent with the orthorhombic phase of $WO_3{\cdot}H_2O$ (JCPDS Card 43-0679). After calcination at 500 °C, the orthorhombic $WO_3{\cdot}H_2O$ is converted into WO_3 with the monoclinic structure (JCPDS card 43-1035), the characteristic peaks of which are (002), (020), and (200), space group is P21/n, (14) and the lattice constants are as follows: a = 7.297 Å, b = 7.539 Å, and c = 7.688 Å. The material composition after calcination can be seen from the corresponding EDS and mapping spectra (see SI Figures S1 and S2).

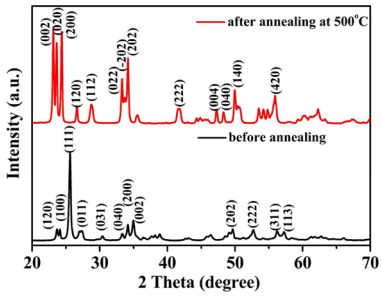

Figure 1. XRD patterns of $WO_3{\cdot}H_2O$ precursor before annealing, and WO_3 material obtained after annealing at 500 °C.

The morphology of the hydrothermal products was characterized by FESEM, as shown in Figure 2. It can be

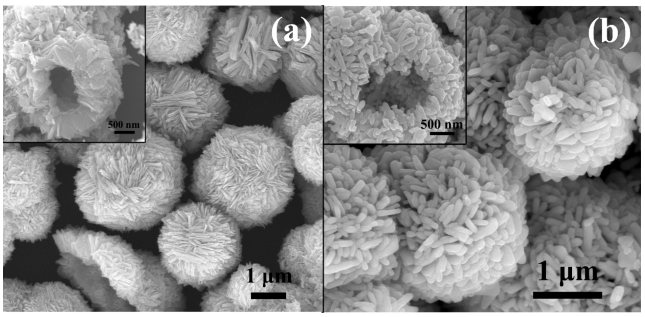

Figure 2. Low and high magnification (inset) FESEM image of (a) the product before annealing, and (b) the WO_3 material obtained after annealing the precursor at 500 °C.

seen that the hydrothermal product consists of hierarchical spheres with diameter of approximately 3 μm. Moreover, parts of the spheres have holes and expose internal cavities, which directly proves that the $WO_3{\cdot}H_2O$ spheres are hollow. The inset image in Figure 2a also confirms their hollow structure and reveals that the hollow sphere consists of a large number of the nanosheets and the thickness of the nanosheet is about 30–50 nm. The material morphology after calcination at 500 °C for 1 h is shown in Figure 2b. It is clear that the hierarchical sphere-like structure still remained. Nanosheets gradually become rounder and the nanosheets become thicker (50–70 nm) after the calcination treatment. The calcination does not change the hollow structure of the spheres, as demonstrated in the inset of Figure 2b.

The nitrogen adsorption and desorption curves of the hierarchical WO_3 HS are shown in Figure 3. Surface area of the

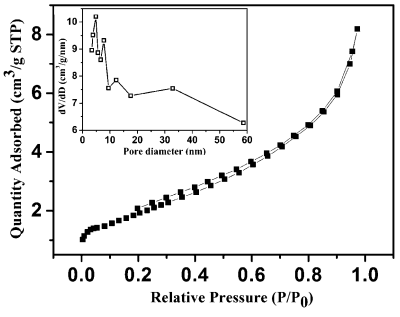

Figure 3. Nitrogen adsorption–desorption isotherm and pore-size distribution curve (inset) of WO_3.

DOI: 10.1021/am508121p
ACS Appl. Mater. Interfaces 2015, 7, 10108–10114

hierarchical WO_3 HS is calculated to be 7 m^2g^{-1}. The pore size distribution of this sample is shown in the inset of Figure 3. We can see that the pore-size distribution curve has four peaks at about 5, 8, 13, and 33 nm, respectively, and displays porous structures with a wide range of pore size distributions from 3 to 60 nm. The porous structure is due to the void space between interweaved nanosheets, as with the FESEM analysis.

The structures of the hierarchical WO_3 HS were further characterized by TEM. Figure 4 displays the HRTEM and

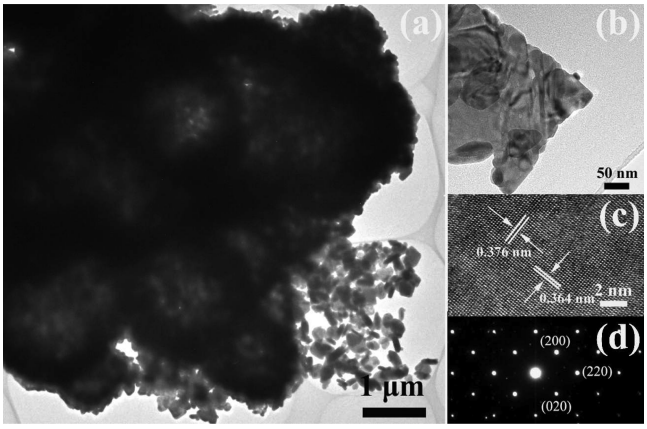

Figure 4. (a) Typical TEM image of the nanosheets self-assembled hierarchical WO_3 HS material. (b) TEM image of a single nanosheet from the cracked hollow structures. (c) HRTEM image of a part of the nanosheet in (b). (d) Corresponding SAED pattern of the WO_3 nanosheet.

TEM images which show the WO_3 material obtained through the calcination treatment of $WO_3{\cdot}H_2O$ at 500 °C in the air. The size and the shape of the hierarchical WO_3 HS are consistent with those observed from FESEM. As seen in Figure 4a, the sharp brightness contrast between centers and the edges of the sphere distinctly confirm that the interior of the WO_3 spheres is hollow. Figure 4b exhibits the TEM image of a single nanosheet, which also proves that the spheres are self-assembled from many nanosheets. Figure 4c presents the HRTEM image of the WO_3 nanosheet. The interplanar spacing of 0.364 and 0.376 nm correspond to (200) and (020) lattice planes of the monoclinic hierarchical WO_3 HS, respectively. The SAED pattern (Figure 4d) demonstrates that the nanosheets have a single crystalline feature.

To understand well the synthesis mechanism of the self-assembled hierarchical HS, the hydrothermal products obtained under different reaction times and amounts of $H_2C_2O_4$ were examined via FESEM, as described below.

Figure 5 shows the FESEM images of the as-synthesized products in different hydrothermal stages, which apparently represents the growing process of the products. It can be seen that numerous irregular nanosheets (with the thickness of ca. 10 nm) are formed in 3 min (Figure 5a). The nanosheets grow further, as shown in Figure 5b. As can be seen in Figure 5c, the spheres (with the diameter ca. 2 μm) start to emerge after being treated for 9 min, while the hierarchical structure on the surface of the spheres is not yet obvious. By the 15th min, the number of spheres is increasing and the spherical hierarchical structure becomes relatively apparent as shown in Figure 5d. During the period between 30 min and 6 h from the start of the treatment, the nanosheets become larger and thicker progressively, and the shape of the nanosheets also becomes

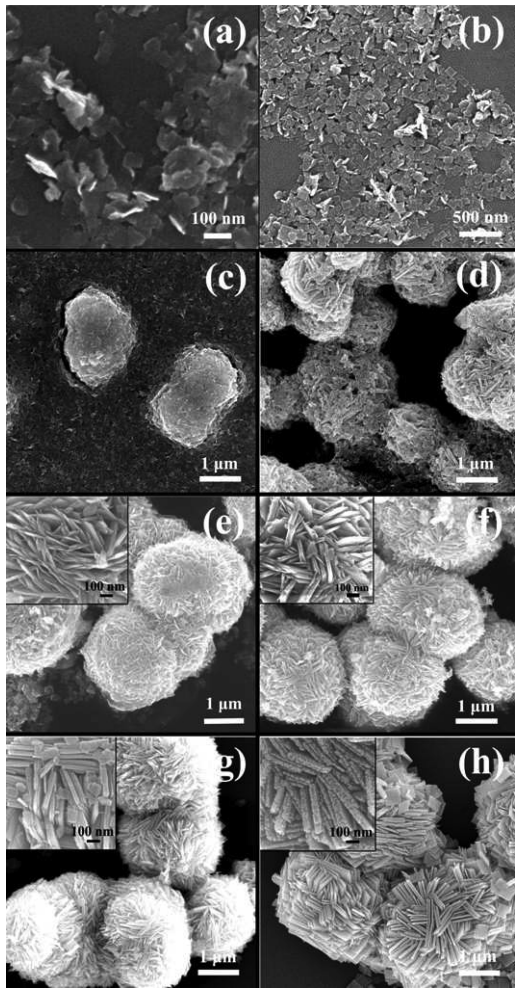

Figure 5. FESEM images of the products synthesized at different growth stages: (a) 3, (b) 6, (c) 9, (d) 15, (e) 30, (f) 60, (g) 180, and (h) 360 min.

more regular, while the size of the spheres almost does not change (Figure 5e–h). After 3 h, the well-defined self-assembled hierarchical HS of $WO_3{\cdot}H_2O$ nanosheets are obtained, as displayed in Figure 5g.

The abbreviations of the molar ratio of $H_2C_2O_4$/sodium tungstate are defined as follows: 0.05:1 = OAST005, 0.1:1 = OAST01, 0.125:1 = OAST0125, 0.25:1 = OAST025, 0.5:1 = OAST05, 1:1 = OAST1. The molar ratio of the $H_2C_2O_4$/sodium tungstate has a crucial effect on the synthesis of the hierarchical $WO_3{\cdot}H_2O$ HS morphology. The FESEM images of the as-obtained products under different $H_2C_2O_4$/sodium tungstate molar ratios are shown in Figure 6. The products of OAST005, OAST01, and OAST0125 present the change from nanosheets to a flower-like structure which consists of nanosheets (Figure 6a–c), while OAST025 mutates into a spherical structure (Figure 6d). From OAST05 to OAST1, the nanosheets of the formed spheres become even more abundant and closer to each other, while the diameters of the spheres almost do not change (Figure 6e and f). On the basis of the above results, the morphology of the products changes from nanosheets to the hierarchical flower-like structure and finally to HS with the increased content of $H_2C_2O_4$, which confirms that the degree of polymerization also increases with the increase of $H_2C_2O_4$.

DOI: 10.1021/am508121p
ACS Appl. Mater. Interfaces 2015, 7, 10108–10114

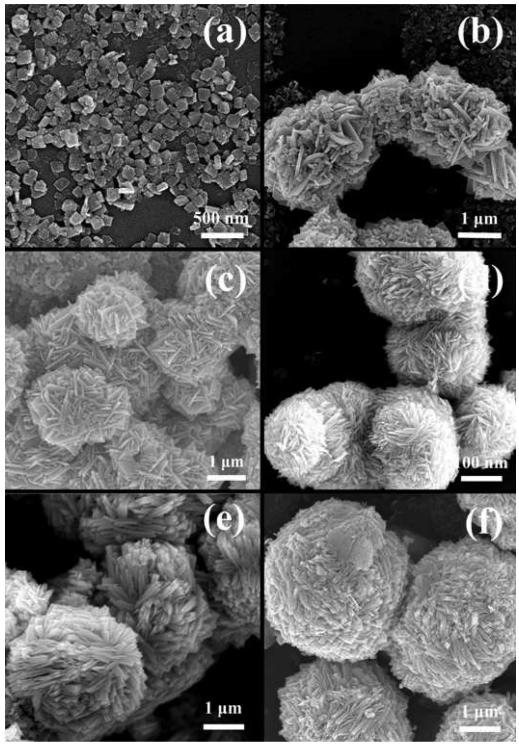

Figure 6. FESEM images of the products synthesized at different molar ratio of $H_2C_2O_4$ to sodium tungstate: (a) 0.05:1, (b) 0.1:1, (c) 0.125:1, (d) 0.25:1, (e) 0.5:1, and (f) 1:1.

3.2. Synthesis Mechanism of Self-Assembled Hierarchical HS. On the basis of the above results, the possible synthesis mechanism of the self-assembled hierarchical WO_3 HS structure is schematically shown in Figure 7. As shown at the top of the scheme (green arrows), the yellow tungsten acid colloid is obtained by adding HCl into the sodium tungstate solution, as precursors. The colloidal particles aggregate by oriented attachment and form the sheet structure in the hydrothermal process. As shown at the bottom of the scheme (blue arrows), $H_2C_2O_4$ as the chelating agent is added to the precursors, which controls and slows down the nucleation rate. The yellow colloid turns to the colorless tungsten oxalic coordination compound solution after the addition of $H_2C_2O_4$. The sheet structure forms the coordination compound by polymerization. The nanosheets self-assemble into the sphere structure later. Ostwald ripening is responsible for the formation of the hollow structure. The shell growth is accompanied by the disappearance of inner small particles, increase of the reaction time, and thus formation of self-assembled hierarchical HS from nanosheets.[22−24]

The hollow structure is related to the concentration of $H_2C_2O_4$. Figure 8 presents typical TEM images of the obtained

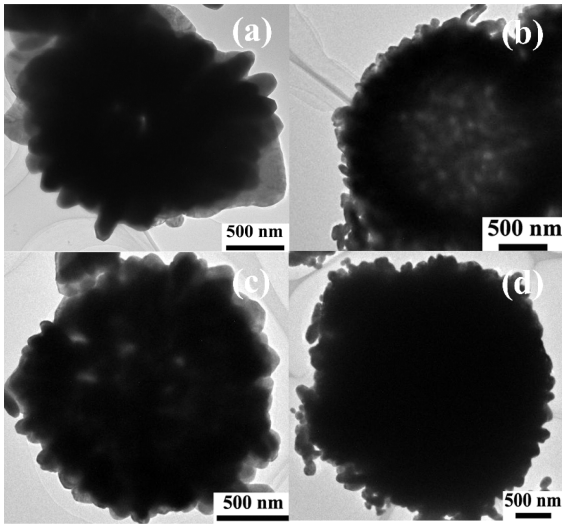

Figure 8. TEM images of WO_3 hierarchical spheres obtained at different molar ratios of the $H_2C_2O_4$ to sodium tungstate: (a) 0.125:1, (b) 0.25:1, (c) 0.5:1, and (d) 1:1.

materials by the calcination treatment of OAST0125, OAST025, OAST05, and OAST1 product at 500 °C. Figure 8a shows the hierarchical flower-like structure that is made up of many nanosheets, as was also demonstrated from the above FESEM results (Figure 6c). Figure 8b also confirms that the sphere of WO_3 obtained from OAST025 is the hollow structure as can be seen from the above FESEM (Figure 2b) and TEM (Figure 4a) results. Figure 8c displays the brightness contrast in the sphere, which demonstrates that the sphere of WO_3 obtained from OAST05 is hollow in some position. The image shown in Figure 8d suggests that the sphere of WO_3 obtained from OAST1 is apparently a solid structure. It can be seen from Figure 8 that the difference of hollow degree is

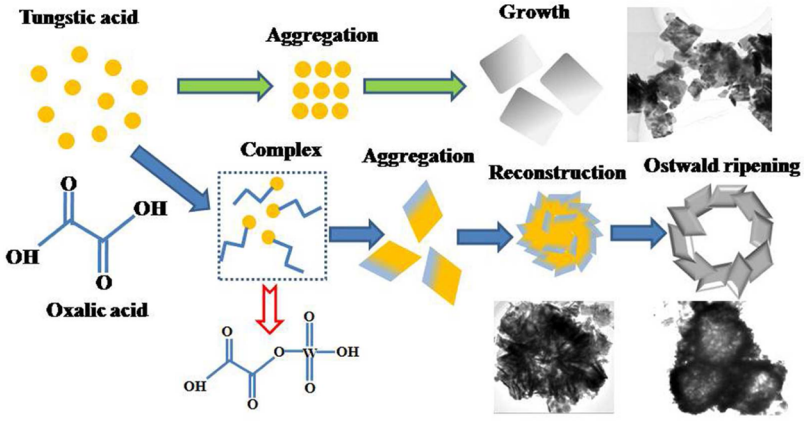

Figure 7. Schematic illustration of the synthesis route and mechanism of the material in the presence of oxalic acid and without oxalic acid conditions, respectively.

DOI: 10.1021/am508121p
ACS Appl. Mater. Interfaces 2015, 7, 10108−10114

affected by the concentration of $H_2C_2O_4$. The $H_2C_2O_4$ with high concentration leads to the high degree of condensation.

3.3. Gas Sensing Properties. *3.3.1. Properties Measurement.* The gas sensing properties of the self-assembled hierarchical WO_3 HS (obtained by calcination of precursor at 500 °C) were investigated. The response performance of WO_3 HS was tested at 140 °C, as shown in Figure 9a. The resistance

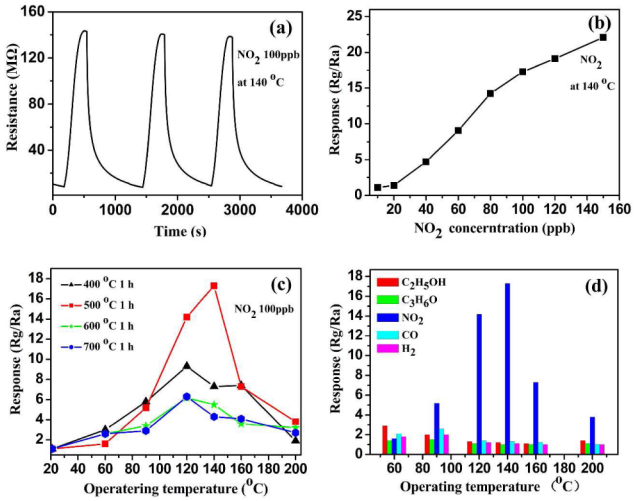

Figure 9. (a) Response and recovery curves of the hierarchical WO_3 HS to 100 ppb NO_2 after 3 cycles of gas on and off at 140 °C. (b) Response curve of the hierarchical WO_3 HS to different concentrations of NO_2 ranging from 10 to 150 ppb and measured at 140 °C. (c) Responses of WO_3 material calcined at different temperatures to 100 ppb NO_2 at different operating temperatures. (d) Responses of the material to various gases at different operating temperatures.

variation of WO_3 HS is reproducible for repeated testing cycles, as the material holds its amplitude of the initial response without an obvious change for the successional three tests to 100 ppb NO_2, and maximum sensitivity reaches ~18. The WO_3 HS exhibits excellent response and reproducibility. Furthermore, the response versus NO_2 concentration was examined (Figure 9b). The NO_2 concentration test ranges from 10 to 150 ppb. The responses of the sensing material increase with the increase of the NO_2 concentration. When the NO_2 concentration is 150 ppb, the response is up to 22.6. Figure 9c presents the response of the obtained WO_3 materials by calcination at different temperatures to 100 ppb NO_2, which is regarded as the function of working temperatures. The response of the material is significantly affected by the working temperature. For WO_3 HS calcinated at 500 °C, the sensitivity increases continuously with the increase of the working temperature that is changed from room temperature to 140 °C, and then it decreases. The maximum response (approaches to ~18) is measured at the optimum working temperature, which is 140 °C. The maximum response of the material after the calcination treatment at 500 °C is apparently much higher than that for the others. Hence, the optimal calcination condition of 500 °C was selected for the WO_3 sensing device to detect continuously its gas sensing performance. As it is well-known, selectivity is also an indispensable parameter for a gas sensing device. Figure 9d demonstrates the bar graph of the response of WO_3 to different gases, among which are ethanol, acetone, H_2, and CO, at a concentration of 10 ppm, while NO_2 concentration is 100 ppb. These results indicate that hierarchical WO_3 HS demonstrates higher response and superior selectivity to NO_2 relative to other examined gases.

3.3.2. Properties Analysis. The gas sensing properties are influenced by the hierarchical WO_3 HS structure. This structure depends on the calcination temperature and the dosage of $H_2C_2O_4$. Figure 10 shows FESEM images of WO_3 materials

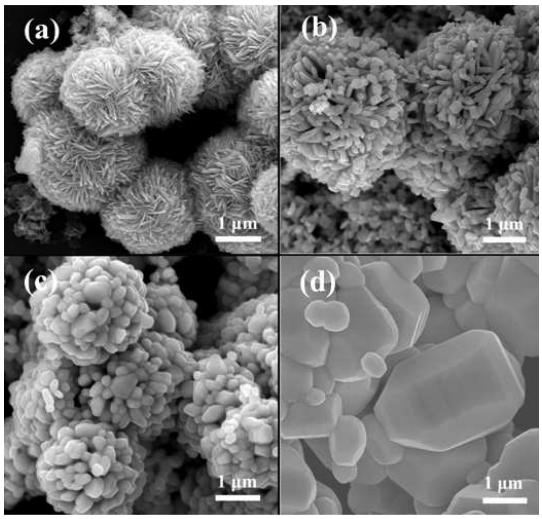

Figure 10. FESEM images of the $WO_3 \cdot H_2O$ products calcined at (a) 400, (b) 500, (c) 600, and (d) 700 °C in air for 1 h.

calcinated at various temperatures in air for 1 h. It clearly demonstrates that sphere-like structures still remain, despite the calcination temperature increase from 400 to 600 °C (Figure 10a–c). Nevertheless, at 700 °C, sphere-like structures completely disappeared, and were replaced by large particles (Figure 10d). According to the above information, when the calcination temperature reaches 600 and 700 °C (Figure 10c and d), the materials are further fusing and the hierarchical hollow structure is gradually destroyed, which causes reduction of the surface area, which in turn leads to degradation of the gas sensing properties. As for the WO_3 calcinated at 400 °C, the obtained materials have poor crystallinity and purity caused by incomplete carbonization of oxalate, which influences the gas sensing properties. XRD patterns of the obtained materials calcinated at different temperatures are shown in Figure S3 in the SI. The WO_3 product calcinated at 500 °C has high crystallinity and complete hollow structure, which may be the main cause of the high sensitivity.

From the above discussion, hollow structure plays an important role in gas sensing properties. The response curves in Figure 11 further confirm the enhancement effect of the hollow structure on the gas sensing properties to 100 ppb NO_2 at 140 °C. The OAST025 has excellent sensitivity, which can possibly be ascribed to the hierarchical HS structure. However, OAST01, OAST0125, OAST05, and OAST1 do not have the complete hollow structure as can be seen from TEM images in Figure 8, therefore, their sensitivity is lower.

3.4. Gas Sensing Mechanism. The proposed mechanism of the gas sensing performance is based on the sensing material's conductivity. When the WO_3 sensor is placed in the air, plenty of O_2 is adsorbed by the active sites. O_2 further attracts electrons near the active sites of WO_3 surface, which gives rise to the several types of adsorption states (O_2^-, O^-, or O^{2-}). In consequence, the depletion zone of the electron corresponding to the adsorption states around the surface area

DOI: 10.1021/am508121p
ACS Appl. Mater. Interfaces 2015, 7, 10108–10114

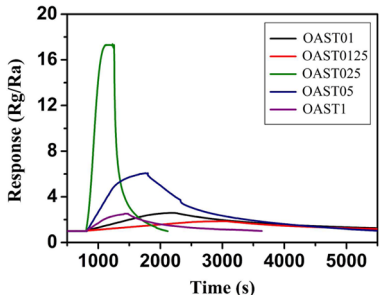

Figure 11. Responses of WO_3 sensing materials obtained at different $H_2C_2O_4$ dosages toward 100 ppb NO_2.

of WO_3 HS emerges. The resistance of WO_3 HS is changed by transferring electrons to O_2. When the sensor is transferred to the NO_2 atmosphere, the situation is different. Because NO_2 gas possesses relatively strong electrophilic property, it can seize electrons from the energy band of WO_3 HS and adsorbed oxygen ions, further forming $NO_2^-{}_{(ads)}$. Specific reactions are as follows:[25]

$$NO_{2(gas)} + e^- \rightarrow NO_2^-{}_{(ads)} \quad (1)$$

$$NO_{2(gas)} + O^-_{2(ads)} + 2e^- \rightarrow NO_2^-{}_{(ads)} + 2O^-{}_{(ads)} \quad (2)$$

The equations above indicate that the resistance of WO_3 HS material also could be increased through further contributing electrons to NO_2, which leads to a significant reduction of the electrons concentration. Ultimately the sensor resistance increases significantly. $NO_2^-{}_{(ads)}$ begins to be desorbed after NO_2 supply is stopped, and the desorption reaction equation is as follows:

$$NO_2^-{}_{(ads)} + 2O^-{}_{(ads)} + e^- \rightarrow NO_{2(gas)} + 2O^{2-}{}_{(ads)} \quad (3)$$

Eventually, a cycle of measurement becomes true. Reaction recovers to the original condition. The cyclic measurement continues, so the NO_2 detection is achieved.[25] The improvement of the gas sensing properties on the HS WO_3 structure can be referred to the high surface area and the hierarchical hollow structure. Plenty of active sites on the large surface area of WO_3 HS offer a considerable zone for the target gas reaction on the material surface, thereby improving the sensitivity to NO_2. At the same time, the porous structure between interlaced nanosheets promotes diffusion of the target gas molecules in materials, helping to realize the rapid response.

4. CONCLUSIONS

Summarizing, we demonstrated that a one-step synthesis approach involving hydrothermal conditions can be successfully applied to obtain hierarchical HS of WO_3. Such hierarchical hollow structures can enhance the sensitivity to NO_2, which is due to the large specific surface area that accelerates the gas diffusion. The optimal process for obtaining the hierarchical WO_3 HS was found to be calcination at 500 °C for 1 h. The performance measurements illustrate that the WO_3 HS exhibits the response as high as 18 to 100 ppb at 140 °C. Response and recovery times for 100 ppb NO_2 were estimated to be 90 and 400 s, respectively. Cross-comparison indicates that the WO_3 HS has preferable selectivity to NO_2. In this paper, oxalic coordination compound adjusts the hydrothermal nucleation rate, which further controls the morphology of the hydrothermal products, and ultimately forms self-assembled HS structures. Our work presents an original and effective method for production of WO_3 gas sensing materials that can be used for improvement of the gas sensors' performance.

■ ASSOCIATED CONTENT

Ⓢ Supporting Information

Experimental parameters of various products, EDS and mapping spectra of the material, and XRD of the products calcined at different temperature. The Supporting Information is available free of charge on the ACS Publications website at DOI: 10.1021/am508121p.

■ AUTHOR INFORMATION

Corresponding Author

*E-mail: xiaohan2298@163.com. Phone: +86-0451-88060349.

Notes

The authors declare no competing financial interest.

■ ACKNOWLEDGMENTS

This work was partially supported by the Natural Science Foundation of China (61403110), and Science and Technology Research Project of Heilongjiang Province Department of Education, China (12541224)

■ REFERENCES

(1) Li, W. J.; Fu, Z. W. Nanostructured WO_3 Thin Film as a New Anode Material for Lithium-ion Batteries. *Appl. Surf. Sci.* **2010**, *256*, 2447−2452.

(2) Huang, J. R.; Xu, X. J.; Gu, C. P.; Fu, G. J.; Wang, W. Z.; Liu, J. H. Flower-like and Hollow Sphere-like WO_3 Porous Nanostructures Selective Synthesis and Their Photocatalysis Property. *Mater. Res. Bull.* **2012**, *47*, 3224−3232.

(3) Zheng, H. D.; Tachibana, Y.; Kalantar-zadeh, K. Dye-Sensitized Solar Cells Based on WO_3. *Langmuir* **2010**, *26*, 19148−19152.

(4) Zoontjes, M. G.; Huijben, M.; Baltrusaitis, J.; Vander Wiel, W. G.; Mul, G. Selective Hydrothermal Method to Create Patterned and Photoelectrochemically Effective Pt/WO_3 Interfaces. *ACS Appl. Mater. Interfaces* **2013**, *5*, 13050−13054.

(5) Park, S. H.; An, S. Y.; Ko, H. S.; Jin, C. H.; Lee, C. M. Synthesis of Nanograined ZnO Nanowires and Their Enhanced Gas Sensing Properties. *ACS Appl. Mater. Interfaces* **2012**, *4*, 3650−3656.

(6) Chen, D.; Xu, J.; Xie, Z.; Shen, G. Z. Nanowires Assembled SnO_2 Nanopolyhedrons with Enhanced Gas Sensing Properties. *ACS Appl. Mater. Interfaces* **2011**, *3*, 2112−2117.

(7) Van, P. T. H.; Thanh, N. H.; Quang, V. V.; Duy, N. V.; Hoa, N. D.; Hieu, N. V. Scalable Fabrication of High-Performance NO_2 Gas Sensors Based on Tungsten Oxide Nanowires by On-Chip Growth and RuO_2-Functionalization. *ACS Appl. Mater. Interfaces* **2014**, *6*, 12022−12030.

(8) Wetchakun, K.; Samerjai, T.; Tamaekong, N.; Liewhiran, C.; Siriwong, C.; Kruefu, V.; Wisitsoraat, A.; Tuantranont, A.; Phanichphant, S. Semiconducting Metal Oxides as Sensors for Environmentally Hazardous Gases. *Sens. Actuators B* **2011**, *160*, 580−591.

(9) Liu, S. Y.; Zhang, F.; Li, H.; Chen, T.; Wang, Y. D. Acetone Detection Properties of Single Crystalline Tungsten Oxide Plates Synthesized by Hydrothermal Method Using Cetyltrimethyl Ammonium Bromide Supermolecular Template. *Sens. Actuators B* **2012**, *162*, 259−268.

(10) Zhang, H. B.; Yao, M. S.; Bai, L. Y.; Xiang, W. C.; Jin, H. C.; Li, J. L.; Yuan, F. L. Synthesis of Uniform Octahedral Tungsten Trioxide by RF Induction Thermal Plasma and Its Application in Gas Sensing. *CrystEngComm* **2013**, *15*, 1432−1438.

(11) Ponzoni, A.; Russo, V.; Bailini, A.; Casari, C. S.; Ferroni, M.; Bassi, A. L.; Migliori, A.; Morandi, V.; Ortolani, L.; Sberveglieri, G.; Bottani, C. E. Structural and Gas-Sensing Characterization of

DOI: 10.1021/am508121p
ACS Appl. Mater. Interfaces 2015, 7, 10108−10114

Tungsten Oxide Nanorods and Nanoparticles. *Sens. Actuators B* **2011**, *153*, 340−346.
(12) Kukkola, J.; Mohl, M.; Leino, A. R.; Mäklin, J.; Halonen, N.; Shchukarev, A.; Konya, Z.; Jantunen, H.; Kordas, K. Room Temperature Hydrogen Sensors Based on Metal Decorated WO_3 Nanowires. *Sens. Actuators B* **2013**, *186*, 90−95.
(13) Chen, X. Y.; Zhou, Y.; Liu, Q.; Li, Z. D.; Liu, J. G.; Zou, Z. G. Ultrathin, Single-Crystal WO_3 Nanosheets by Two-Dimensional Oriented Attachment toward Enhanced Photocatalystic Reduction of CO_2 into Hydrocarbon Fuels under Visible Light. *ACS Appl. Mater. Interfaces* **2012**, *4*, 3372−3377.
(14) Qiu, Y. C.; Xu, G. L.; Kuang, Q.; Sun, S. G.; Yang, S. H. Hierarchical WO_3 Flowers Comprising Porous Single-Crystalline Nanoplates Show Enhanced Lithium Storage and Photocatalysis. *Nano Res.* **2012**, *5*, 826−832.
(15) Cui, J. C.; Sun, J. B.; Liu, X.; Li, J. W.; Ma, X. Z.; Chen, T. T. Fabrication of Hierarchical Flower-like Porous ZnO Nanostructures from Layered $ZnC_2O_4{\cdot}3Zn(OH)_2$ and Gas Sensing Properties. *Appl. Surf. Sci.* **2014**, *308*, 17−23.
(16) Anoshkin, I. V.; Nasibulin, A. G.; Mudimela, P. R.; He, M. S.; Ermolov, V.; Kauppinen, E. I. Single-Walled Carbon Nanotube Networks for Ethanol Vapor Sensing Applications. *Nano Res.* **2013**, *6*, 77−86.
(17) Cagliani, A.; Mackenzie, D. M. A.; Tschammer, L. K.; Pizzocchero, F.; Almdal, K.; Bøggild, P. Large-area Nanopatterned Graphene for Ultrasensitive Gas Sensing. *Nano Res.* **2014**, *7*, 743−754.
(18) Liu, X.; Cui, J. S.; Sun, J. B.; Zhang, X. T. 3D Graphene Aerogel-Supported SnO_2 Nanoparticles for Efficient Detection of NO_2. *RSC Adv.* **2014**, *4*, 22601−22605.
(19) Hoa, N. D.; Duy, N. V.; Hieu, N. V. Crystalline Mesoporous Tungsten Oxide Nanoplate Monoliths Synthesized by Directed Soft Template Method for Highly Sensitive NO_2 Gas Sensor Applications. *Mater. Res. Bull.* **2013**, *48*, 440−448.
(20) Li, X. L.; Lou, T. J.; Sun, X. M.; Li, Y. D. Highly Sensitive WO_3 Hollow-Sphere Gas Sensors. *Inorg. Chem.* **2004**, *43*, 5442−5449.
(21) Lou, X. W.; Archer, L. A.; Yang, Z. C. Hollow Micro-Nanostructures: Synthesis and Applications. *Adv. Mater.* **2008**, *20*, 3987−4019.
(22) Bai, S. L.; Zhang, K. W.; Wang, L. S.; Sun, J. H.; Luo, R. X.; Li, D. Q.; Chen, A. F. Synthesis Mechanism and Gas-Sensing Application of Nanosheet-Assembled Tungsten Oxide Microspheres. *J. Mater. Chem. A* **2014**, *2*, 7927−7934.
(23) Li, L. Z.; Zhao, J. Z.; Wang, Y.; Li, Y. L.; Ma, D. C.; Zhao, Y.; Hou, S. G.; Hao, X. L. Oxalic Acid Mediated Synthesis of $WO_3{\cdot}H_2O$ Nanoplates and Self-Assembled Manoflowers under Mild Conditions. *J. Solid State Chem.* **2011**, *184*, 1661−1665.
(24) Bai, S. L.; Zhang, K. W.; Luo, R. X.; Li, D. Q.; Chen, A. F.; Liu, C. C. Sonochemical Synthesis of Hierarchically Assembled Tungsten Oxides with Excellent NO_2-Sensing Properties. *Mater. Lett.* **2013**, *111*, 32−34.
(25) Bai, S. L.; Zhang, K. W.; Luo, R. X.; Li, D. Q.; Chen, A. F.; Liu, C. C. Low-temperature Hydrothermal Synthesis of WO_3 Nanorods and Their Sensing Properties for NO_2. *J. Mater. Chem.* **2012**, *22*, 12643−12650.

DOI: 10.1021/am508121p
ACS Appl. Mater. Interfaces 2015, 7, 10108−10114